· Article · Advances in Polar Science
doi: 10.13679/j.advps.2019.1.00052 March 2019 Vol. 30 No. 1: 52-69

Constraints on early Paleozoic magmatic processes and tectonic setting of Inexpressible Island, Northern Victoria Land, Antarctica

CHEN Hong[1,2*], WANG Wei[1,2] & ZHAO Yue[1,2]

[1] Institute of Geomechanics, Chinese Academy of Geological Sciences, Beijing 100081, China;
[2] Key Laboratory of Paleomagnetism and Tectonic Reconstruction of Ministry of Natural Resources, Beijing 100081, China

Received 2 May 2018; accepted 12 February 2019

Abstract During the Cambrian and Ordovician, widespread magmatic activity occurred in the Ross Orogen of central Antarctica, forming the Granite Harbor Intrusives and Terra Nova Intrusive Complex. In the Terra Nova Intrusive Complex, the latest magmatic activity comprised the emplacement of the Abbott Unit (508 Ma) and the Vegetation Unit (~475 Ma), which were formed in different tectonic settings. Owing to their similar lithological features, the tectonic transformation that occurred between the formation of these two units has not been well studied. Through a detailed geological field investigation and geochemical and geochronological analyses, four types of magmatic rock—basalt, syenite, mafic veins, and granite veins—were identified on Inexpressible Island, Northern Victoria Land. Our SHRIMP (Sensitive High Resolution Ion Micro Probe) zircon U–Pb ages of the basalt and the granite veins are 504.7 ± 3.1 and 495.5 ± 4.9 Ma, respectively. Major- and trace-element data indicate a continental-margin island-arc setting for the formation of these two rock types. The zircon U–Pb ages of the syenite and the monzodiorite veins are 485.8 ± 5.7 and 478.5 ± 4.0 Ma, respectively. Major- and trace-element compositions suggest a collisional setting for the former and an intracontinental extensional setting for the latter. These results elucidate the evolution from subduction to collision and intracontinental extension in Northern Victoria Land during the 20 Ma spanning the late Cambrian–Early Ordovician and improve our understanding of the tectonics and evolution of the Ross Orogen in the Transantarctic Mountains.

Keywords **Northern Victoria Land, Ross Orogen, Early Paleozoic magmatism, island-arc, intracontinental extension**

Citation: Chen H, Wang W, Zhao Y. Constraints on early Paleozoic magmatic processes and tectonic setting of Inexpressible Island, Northern Victoria Land, Antarctica. Adv Polar Sci, 2019, 30(1): 52-69, doi: 10.13679/j.advps.2019.1.00052

1 Introduction

The continent of Antarctica consists of three tectonic units: the Transantarctic Mountains, East Antarctica, and West Antarctica (Boger, 2011). The Transantarctic Mountains are represented by the Ross Orogen, which was formed by the early Paleozoic collision of East and West Antarctica (Farabee et al., 1990; Goodge et al., 2001; Boger and Miller, 2004; Elliot and Fanning, 2008; Federico et al., 2009, 2010; Palmeri et al., 2012; Estrada et al., 2016). In addition to causing metamorphism and deformation of Cambrian and Precambrian strata, the Ross Orogeny was accompanied by large-scale granite intrusions (Giacomini et al., 2007; Federico et al., 2009, 2010; Paulsen et al., 2015; Di Vincenzo et al., 2016). These granites are widely distributed, with abundant outcrops from Northern Victoria Land to the Queen Maud Land, Horlick, and Transantarctic mountains

* Corresponding author, E-mail: chenhong@geomech.ac.cn

(Rocchi et al., 1998; Giacomini et al., 2007; Paulsen et al., 2007; Hagen-Peter and Cottle, 2016). The Granite Harbor Intrusives to the southeast of McMurdo Sound and the Terra Nova Complex of Northern Victoria Land are the most typical granitic mass (Rocchi et al., 1998). The Granite Harbor Intrusives are composed of granite, granodiorite, and tonalite and have ages between 515 and 478 Ma (Vetter and Tessensohn, 1987; Giacomini et al., 2007). Magmatic activity in the Terra Nova Complex also occurred at 510–490 Ma (Black and Sheraton, 1990; Giacomini et al., 2007; Wang et al., 2014). This age range is similar to that of the Granite Harbor Intrusives and other igneous rocks that formed mostly between 515 and 450 Ma, including the Vida and Vanda granites in South Victoria Land (Jones and Faure, 1967), the Theseus granodiorite in the Wright Valley (Hagen-Peter and Cottle, 2016), the Hope granite in the central Transantarctic Mountains, and the Martin Dome in the Miller Range, east of the Queen Elizabeth Range (Paulsen et al., 2013). All of these magmatic events were associated with the Ross Orogeny, with intrusions occurring in the Cambrian and Ordovician periods, and thus represent the intrusive activity of granitic magma during the syn-tectonic and post-tectonic stages of the Ross Orogeny (Giacomini et al., 2007).

Of these intrusions, the Terra Nova Complex was formed in a continental-margin environment (Rocchi et al., 1998). Its most recent magmatic processes formed the Vegetation Unit (~475 Ma) and Abbott Unit (508 Ma), which have different source regions and intrusion depths but possess nearly identical rock compositions including granite, syenite, and mafic veins (Borg et al., 1986; Borsi et al., 1995; Vincenzo and Rocchi, 1999; Perugini et al., 2005). The Abbott Unit was derived from partially melted mantle wedge above the subduction zone mixing with the continental lithospheric mantle, whereas the Vegetation Unit was derived from partially melted ancient sub-continental lithospheric mantle mixing with crustal material under thinning lithosphere within the orogen (Vincenzo and Rocchi, 1999).

The extensive magmatic rocks in the region have been dated at 497–485 Ma and may also represent emplacement/crystallization under an extensional setting (Wang et al., 2014; Rocchi et al., 2015). However, because the Vegetation Unit and Abbott Unit are nearly identical in their lithological characteristics, there is no clear understanding of the relationship between different intrusions in the Terra Nova Complex or of the timing of the change in tectonic mechanism controlling their emplacement. For this study, large-scale geological mapping was conducted on Inexpressible Island, Northern Victoria Land, to ascertain the relationships between different magmatic rocks in the study area. In addition, geochemical and geochronological analyses were performed to provide insights into the Ross Orogeny of the Transantarctic Mountains. The results offer new evidence regarding the tectonic characteristics and evolution of the orogen.

2 Geological setting

The Transantarctic Mountains comprise an early Paleozoic

Table 1 Characteristics of the two-layer bedrock and overlying strata of the Transantarctic Mountains (Chen et al., 2008)

Tectonic layer		Strata age	Shackleton Range and Whichaway Nunataks	Pensacola Mountains	Horlick Mountains and eastern Queen Maud Mountains	Beardmore Glacier and Byrd Glacier	Southern Victoria Land	Northern Victoria Land
Overlying strata		Devonian–Triassic Period	Beacon Supergroup	Dover Sandstone	Beacon Supergroup	Beacon Supergroup	Beacon Supergroup	Beacon Supergroup
					Ross Orogeny			
Bedrock		Silurian / Ordovician		Neptune Group				
	Upper tectonic layer	Cambrian	*Blaiklock Glacier sandstone*	Wienes Formation siltstone and shale; Gambacorta Formation volcanic rocks; Nilson limestone	Liv Group / Nimrod Orogeny	Byrd Group; Douglas conglomerate, Dick Formation Shackleton limestone	Asgard Formation gneiss, schist, and marble; Skelton hard sandstone and limestone; Koettlitz Group schist, marble, and gneiss	Bowers Supergroup
	Lower tectonic layer	Precambrian	Shackleton Range metasandstone	Patuxent Formation sandstone, slate, and basaltic rock	Goldie Formation, Duncan Formation and La Gorce Formation	Goldie Formation sandstone, mudstone, quartzite, and marble		Robertson Bay Group turbidite; Wilson Group amphibolite, gneiss and schist

orogenic belt known as the Ross Orogen, which consists of basement and overlying strata (Table 1; Talarico and Castelli, 1995; Talarico et al., 1995; Boger and Miller, 2004; Giacomini et al., 2007; Paulsen et al., 2007). The basement of the Transantarctic Mountains consists of two tectonically distinct layers, which are Proterozoic and early Paleozoic in age (Chen et al., 2008). Two major tectonic events occurred during the formation of this dual-tectonic-layer basement: The Nimrod or Beardmore Orogeny during the late Precambrian (1000–630 Ma) and the Ross Orogeny during the early Paleozoic (Goodge et al., 2001; Giacomini et al., 2007). After the Nimrod and Ross orogenies, the Transantarctic Mountains underwent intracontinental orogenic processes and uplift (Stump and Fitzgerald, 1992). The overlying strata are composed of late Paleozoic and younger rocks, which unconformably overlie the basement (Chen et al., 2008).

Northern Victoria Land is located in the region of the Transantarctic Mountains close to the Ross Sea and contains large amounts of early Paleozoic magmatic rocks formed during the Ross Orogeny (Rocchi et al., 1998; Vincenzo and Rocchi, 1999; Giacomini et al., 2007; Hagen-Peter and Cottle, 2016). Magmatic activity and later intracontinental evolution resulted in the uplift and denudation of the crust, which in turn led to the formation of the continental conglomerates and sandstones that unconformably overlie the Cambrian strata. These units are unconformably or disconformably overlain by upper Devonian-Triassic strata named as Beacon Supergroup (Table 1; Elliot and Fanning, 2008).

Northern Victoria Land is composed of three fault-bounded terranes: the Wilson, Bowers, and Robertson Bay terranes. These terranes exhibit strikingly different geological features, rock compositions, deformational features, and metamorphic characteristics (Weaver et al., 1984; Sheraton et al., 1987; Capponi et al., 1999; Goodge et al., 2001; Federico et al., 2010). The late Cambrian–Ordovician granites represented by the Granite Harbor Intrusives are developed only in the Wilson Terrane and intrude into the Neoproterozoic Wilson Group. Devonian granite, represented by the Admiralty Intrusion, is developed only in the Robertson Bay and Bowers terranes and intrudes into the Cambrian–Ordovician Robertson Bay Group and Bowers Supergroup. As such, these intrusions differ markedly from those of the Wilson Terrane in terms of geological evolution and are thus considered to be foreign rocks that accreted onto the Wilson Terrane of East Antarctica after Cambrian sedimentation (Federico et al., 2010). Because folding occurred in all three terranes during the Ross Orogeny, the terranes must have become fused before the Early Ordovician. However, the existence of the extensive Devonian–Carboniferous Admiralty Intrusion in the region indicates that the collision of these terranes and the transition to an intracontinental tectonic setting had occurred by this time. This collision resulted in characteristic magmatic activity in Northern Victoria Land.

Inexpressible Island is located in the south of Terra Nova Bay, at 74°50′–74°57′S, 163°35′–163°46′E. The area of the island is approximately 50 km^2, and it extends north to south in a diamond shape. Priestley Glacier lies to the north, the Nansen Ice Sheet lies to the west and south, and Terra Nova Bay of the Ross Sea lies to the east (Figure 1). The main rock outcrops on the island are the granites, diorites, and meta-granitoids of the Vegetation Unit (Vincenzo and Rocchi, 1999). Petrological and geochronological investigations have indicated that the main rock composition of previously unidentified granitoids is quartz monzonite with a small amount of quartz monzodiorite, with an intrusion age of 484–482 Ma (Early Ordovician; Wang et al., 2014). This age information shows that the Ross Orogeny occurred in Northern Victoria Land prior to the Early Ordovician.

3 Distribution and intrusive relationships of magmatic rocks on Inexpressible Island

Geological mapping was performed mainly in the central part of Inexpressible Island. Bedrock outcrops are limited in the surveyed area, with the four main outcrop areas being located in the northern coastline region, the eastern margin of the bay, the low-altitude southern mountains, and the high-altitude western mountains (Figure 2). Bedrock outcrops consist predominantly of magmatic rocks, but the lithological and vein characteristics of this bedrock vary significantly between regions. The main body of these rocks from the northern coastline region consists of coarse-grained gray porphyritic granite (Figure 3a) that is composed of 30%–35% quartz, 15%–40% microcline, 5%–10% perthite, 20%–40% plagioclase, and 5% biotite (Figure 4a). The phenocrysts are typically feldspars measuring approximately 1.5 cm in size. The matrix is composed of smaller feldspar, quartz, and biotite grains of 0.5–1.0 mm in size. Dark gray, deep-source xenoliths are also found in the granites (Figure 3b). Most of these xenoliths are composed of diorite or gabbro, with clear gabbro or diabase structures. Feldspar and biotite crystals in the xenoliths are generally euhedral, whereas quartz and pyroxene are anhedral (Figure 4b). The main minerals are plagioclase (40%), microcline (20%), and biotite (30%). Small amounts of pyroxene, hornblende, and quartz occupy 5%, 3%, and 2%, respectively, and have equigranular textures and grain sizes of approximately 0.5 mm.

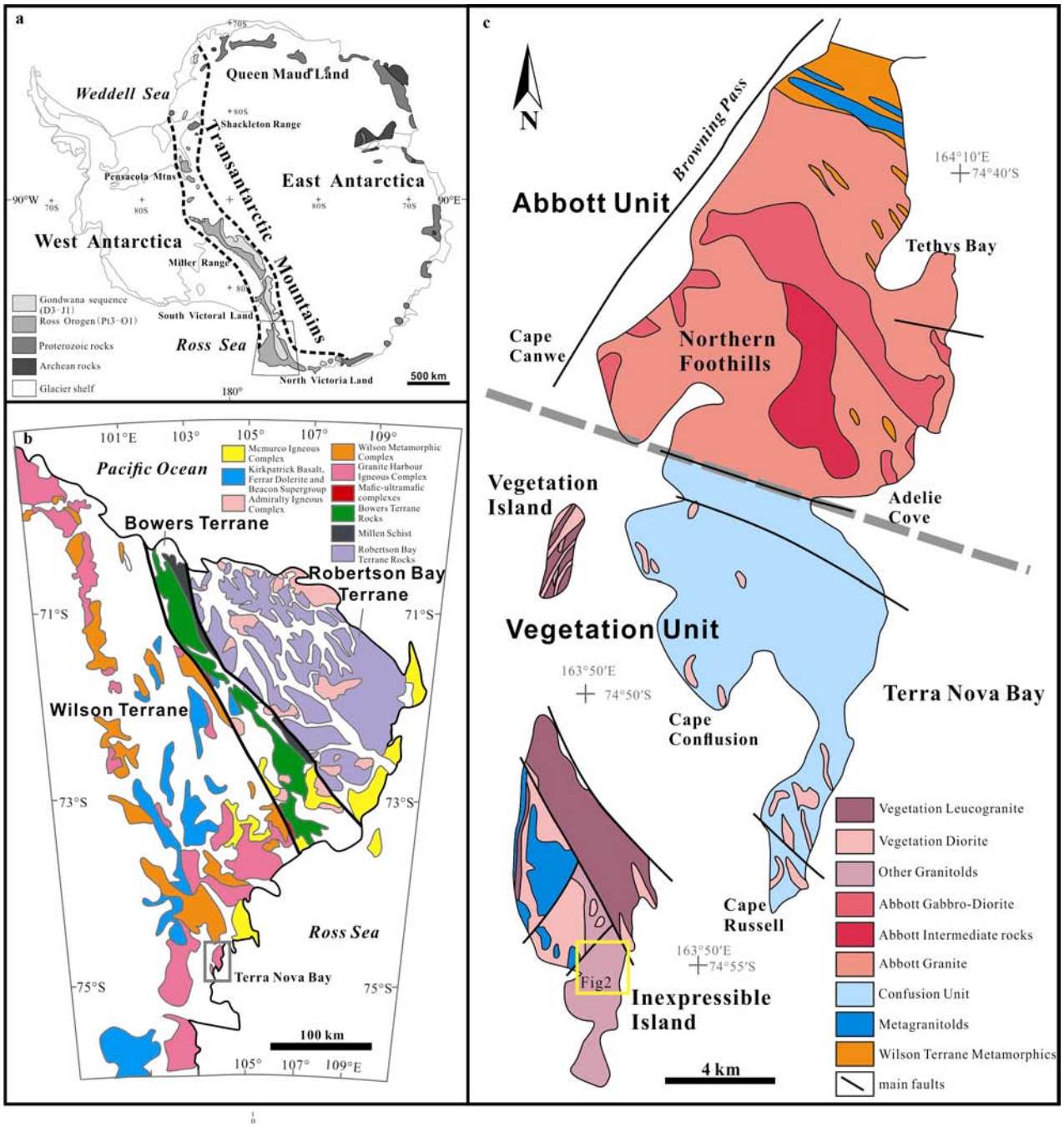

Figure 1 Schematic geological map of Northern Victoria Land and Inexpressible Island (modified after Vincenzo and Rocchi, 1999; Estrada et al., 2016).

Most of the bedrock along the eastern bay is covered by snow and a shallow layer of loose, sandy gravel. The rocks are composed mainly of coarse-grained grayish-white syenite (Figure 3c). The minerals have grain sizes of 2–5 mm and consist of 26% highly euhedral plagioclase, 28% perthite, 33% microcline, 8% biotite, and 4% quartz (Figures 4c–4d). The grains of perthite and microcline are larger than the other minerals, and biotite and quartz are commonly crystallized within the crevices of feldspar grains (Figure 4d). Numerous late-formed gray granite veins crop out in the syenite (Figure 3d). These veins, which trend either NW–SE or NE–SW, are between 0.2 and 20 m in width, and the widest veins trend NNE–SSW (Figure 2). These veins are the same as the granite found in the north coastline region. The orientations of the feldspars and other minerals are the same as those of the vein trends (Figure 3e), which reflects magma flow in the veins. The crystal grains at the centers and edges of the veins are noticeably different in size. The edges contain mainly fine, uniform grains, whereas the centers have porphyritic textures. The phenocrysts are primarily

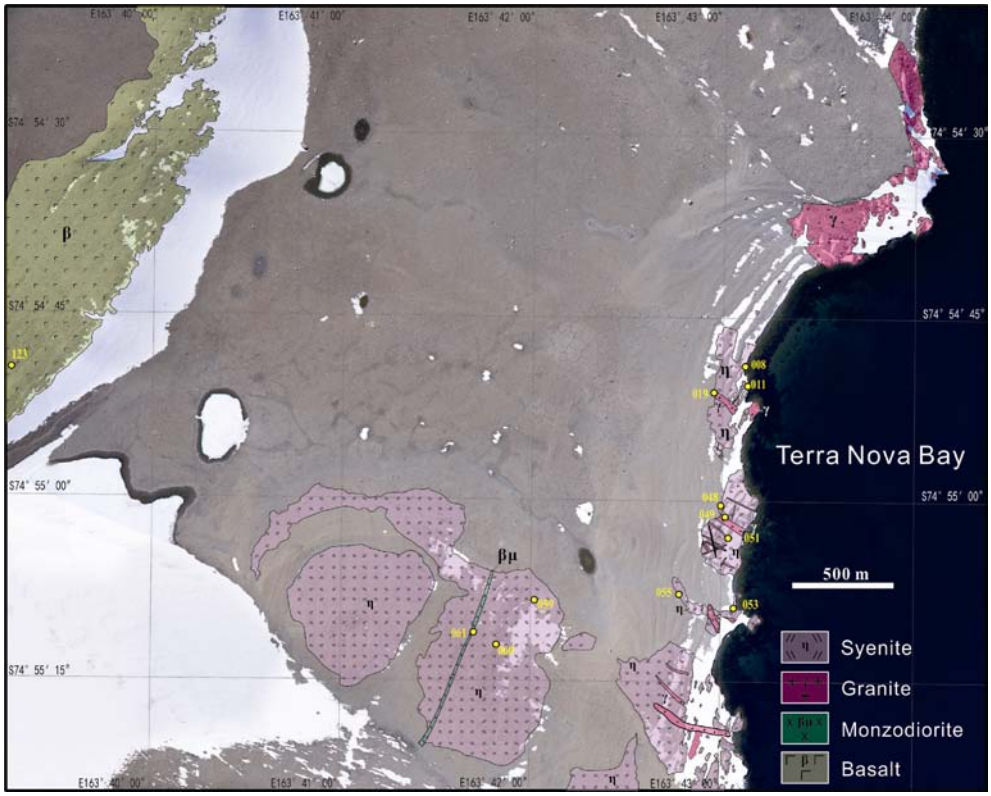

Figure 2 Geological map of central Inexpressible Island, west of Terra Nova Bay. The remote sensing map is an aerial image from the Heilongjiang Bureau of Surveying and Mapping Geoinformation, China.

microcline, demonstrating the late-intrusion characteristics of the vein bodies (Figure 4e).

The bedrock of the low-altitude southern mountains is covered by glacial moraine (Figure 2). The rock outcrops are composed mainly of coarse-grained grayish-white syenite with the same lithological features as those of the main rock at the coastline (Figures 4c–4d). A ~5-m-wide mafic vein occurs with an approximately N–S trend and extends over 300 m across the bedrock outcrop area in the low-altitude southern mountains area (Figure 3f). This vein consists of monzodiorite with porphyritic or diabase structures. The main minerals are 50%–70% plagioclase, 25%–35% biotite, and 5%–10% chloritized and amphibolized pyroxene. The phenocrysts consist predominantly of plagioclase and pyroxene and have grain sizes of ~0.5 mm. The matrix is composed primarily of feldspar and biotite, with small grain sizes of ~50 μm (Figure 4f).

The widely exposed plutons in the western alpine region are dominated by grayish-green basalt (Figure 3g), which shows substantial spheroidal weathering on exposed surfaces and has a massive structure. The main mineral composition of this basalt is 28% plagioclase, 23% pyroxene, 4% olivine, and 45% vitreous and opaque minerals, with notable porous and porphyritic structures (Figures 4g–4h). Phlogopite grains are relatively large and are observable in the field, with grain sizes of ~1 cm. Pyroxene phenocrysts are mostly 2–3 mm in size (Figure 4h). In addition, two veins are found in this area (Figure 3h). The older vein is a N–S-trending diabase vein composed of pyroxene and feldspar that exhibits a strong diabasic texture. The vein is almost parallel to the monzodiorite vein in the low-altitude southern mountains area, and these veins may be coeval. The younger vein is a fine-grained, E–W-trending granite vein.

4 Zircon U–Pb dating

Although the field study revealed the successive relationships of the syenite, monzodiorite, and granite veins, as well as the sequence of the basalt, mafic, and granite veins, it offered no direct evidence of the chronological relationship between the syenite and the basalt. Although laser ablation inductively coupled plasma mass spectrometry (LA–ICP–MS) has been used to determine the ages of the syenite on the island (484–482 Ma; Wang et al., 2014), the intrusion relationships between the different rocks have not been discussed in detail and thus require further geochronological investigation.

For this study, zircon dating was performed on syenite, basalt, and monzodiorite veins intruded into the syenite and on the granite vein intruded into the basalt. Syenite sample VC008/1 was collected from the eastern coast at 74°54′49.0″S, 163°43′07.3″E. Basalt sample

VC123/1 was taken from the western alpine region at 74°54′51.7″S, 163°38′46.7″E. Monzodiorite sample VC61/1 was collected from the low-altitude southern mountains at 74°55′11.0″S, 163°41′42.1″E. Granite sample VC123/3 was taken from the western alpine region at 74°54′51.7″S, 163°38′46.7″E.

All the zircons were separated by hand crushing, washing, and electromagnetic and heavy-liquid techniques and then selected under a binocular microscope to obtain zircons with few inclusions, no obvious cracks, and intact crystals. The zircons were ground in epoxy resin and then polished and cleaned. The cathodoluminescence (CL) imaging of zircons and U–Pb dating were completed in the Beijing SHRIMP Center of the Chinese Academy of Geological Sciences in Beijing, China. The instrument used for the dating is SHRIMP IIe. The standard zircon TEM (t = 417 Ma) was used to correct for inter-element fractionation. The analytical procedure and experimental parameters used followed those of Song et al. (2002), Black et al. (2003), and Liu et al. (2003). The dating results for all the samples are provided in Table 2. The original data were processed using Squid software (Ludwig, 2009).

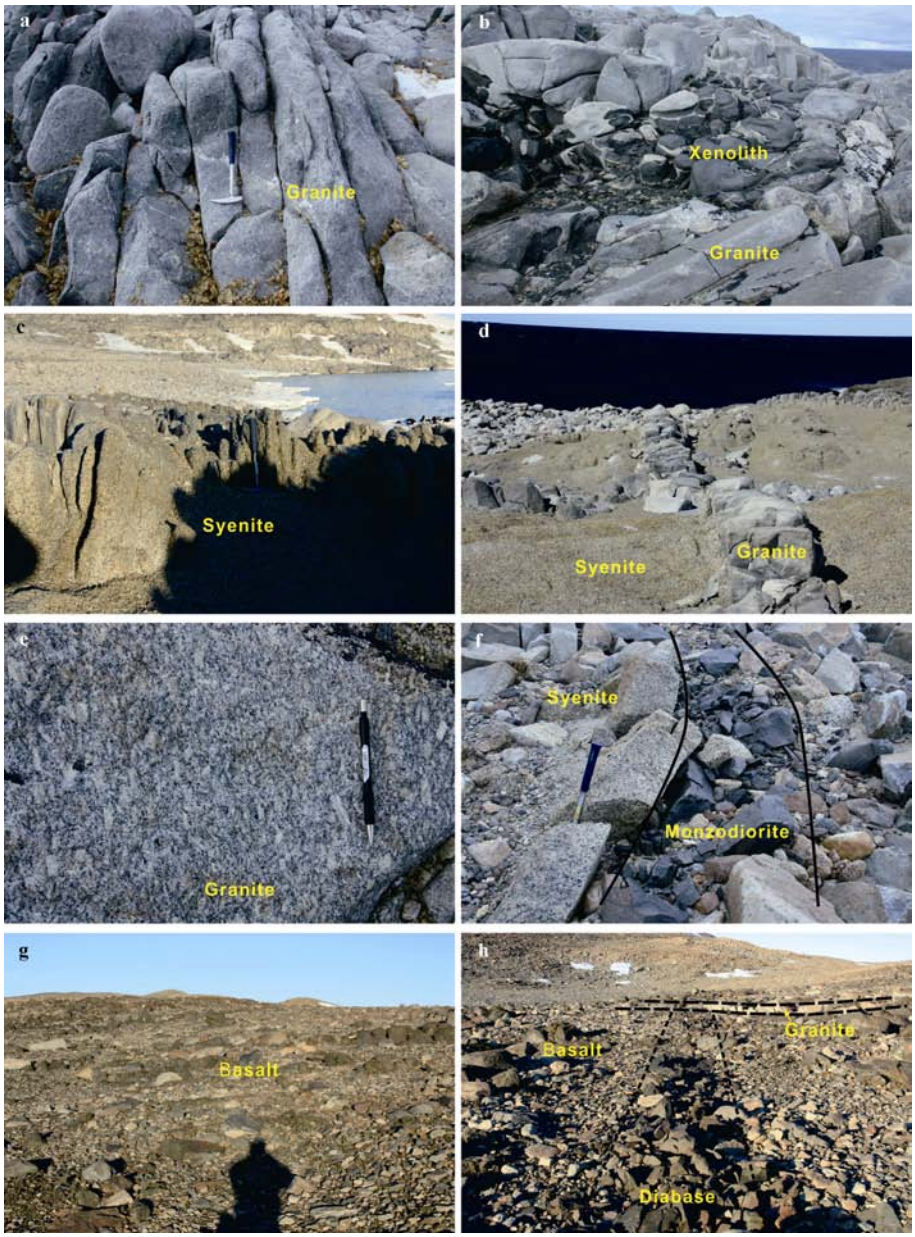

Figure 3 Field characteristics of the Inexpressible Island bedrock. **a**, Granite bedrock in the northern coastline region. **b**, Granite and xenoliths in the northern coastline region. **c**, Syenite bedrock in the eastern bay region. **d**, Syenite and granitic veins in the eastern bay region. **e**, Mineral composition of the granitic veins. **f**, Monzodiorite vein intruded into the syenite in the low-altitude southern mountains. **g**, Basalt bedrock in the western alpine region. **h**, Diabase and granite vein intruded into basalt.

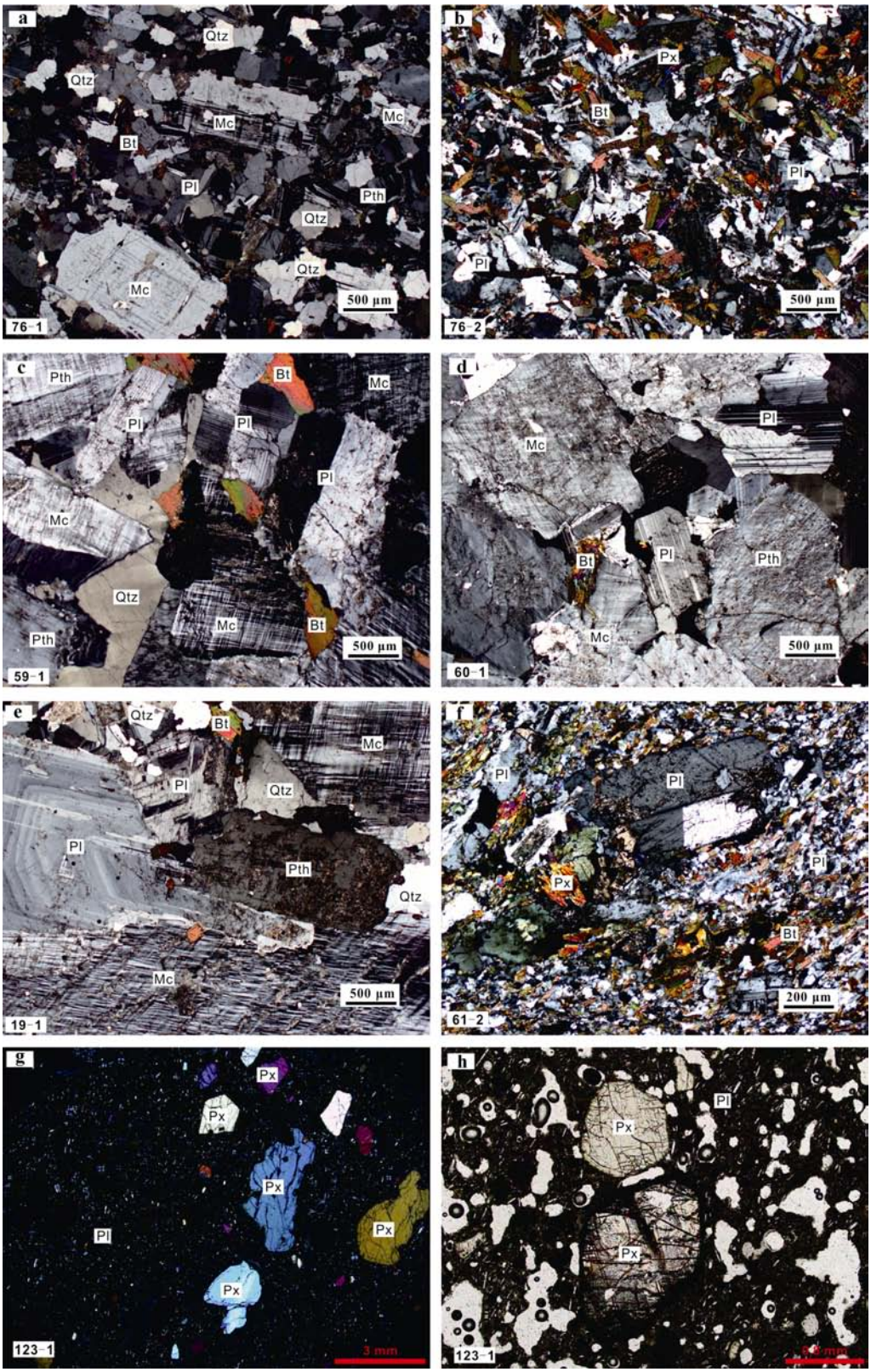

Figure 4 Microscopic characteristics of the rocks from Inexpressible Island. **a**, Granite from the northern coastline region. **b**, Xenolith in the granite. **c** and **d,** Syenite from the eastern bay and low-altitude southern mountains regions. **e**, Granitic vein in the syenite. **f**, Monzodiorite intruded into the syenite. **g** and **h**, Basalt from the western alpine region. Bt: Biotite; Mc: Microcline; Qtz: Quartz; Pl: Plagioclase; Pth: Perthite; Px: Pyroxene.

Table 2 SHRIMP zircon U–Pb data of intrusive rocks, Inexpressible Island, Northern Victoria Land

	Grain. spot	$^{206}Pb_c$ /%	Elem. content ($\times10^{-6}$)			$^{232}Th/^{238}U$	Radiogenic ratios						err corr.	Age/Ma				Conc. /%
			U	Th	$^{206}Pb^*$		$n(^{207}Pb)/n(^{206}Pb)$		$n(^{207}Pb)/n(^{235}U)$		$n(^{206}Pb)/n(^{238}U)$			$n(^{206}Pb)/n(^{238}U)$		$n(^{207}Pb)/n(^{206}Pb)$		
							Value	±/%	Value	±/%	Value	±/%		Value	1σ	Value	1σ	
VC008/1 Syenite	VC008-1.1	1.20	70	53	4.84	0.78	0.0598	9.7	0.653	9.9	0.0792	2.2	0.225	491.0	11	597	210	82
	VC008-2.1	2.05	78	49	5.19	0.66	0.0467	18.0	0.491	18.0	0.0763	2.3	0.125	474.0	10	32	440	1481
	VC008-3.1	0.62	59	45	3.95	0.79	0.0609	15.0	0.648	15.0	0.0772	2.6	0.172	479.0	12	635	310	75
	VC008-4.1	--	44	22	2.97	0.52	0.0699	6.9	0.762	8.1	0.079	4.3	0.531	490.0	20	926	140	53
	VC008-5.1	--	80	59	5.53	0.77	0.0712	7.3	0.801	7.8	0.0816	2.8	0.359	506.0	14	963	150	53
	VC008-6.1	3.35	38	21	2.52	0.57	0.0460	20.0	0.478	21.0	0.0754	3.1	0.152	469.0	14	−2	490	−23450
	VC008-7.1	0.20	82	61	5.65	0.77	0.0616	16.0	0.680	16.0	0.0798	2.1	0.128	494.9	9.9	659	350	75
	VC008-8.1	1.75	42	27	2.77	0.68	0.0555	12.0	0.584	13.0	0.0763	2.4	0.191	474.0	11	432	280	110
	VC008-9.1	--	79	60	5.3	0.78	0.0690	16.0	0.740	17.0	0.0786	2.2	0.134	488.0	10	886	340	55
	VC008-10.1	0.00	87	63	5.77	0.75	0.0582	5.4	0.623	5.7	0.0776	1.7	0.296	481.9	7.8	539	120	89
	VC008-11.1	0.00	74	54	5.08	0.75	0.0600	4.2	0.665	4.7	0.0804	2	0.428	498.2	9.6	604	91	82
	VC008-12.1	1.25	62	47	4.32	0.78	0.0554	13.0	0.607	14.0	0.0795	2.1	0.157	493.0	10	429	300	115
	VC008-13.1	2.29	73	55	4.92	0.78	0.0486	20.0	0.510	20.0	0.0761	2.1	0.104	473.0	9.6	129	470	367
	VC008-14.1	0.84	62	49	4.28	0.81	0.0591	14.0	0.647	15.0	0.0793	2.2	0.149	492.0	10	572	310	86
VC061/1 Monzo-diorite Vein	VC061-1.1	--	409	232	28.4	0.59	0.0588	1.9	0.656	2.1	0.0809	0.9	0.435	501.5	5.0	560	42	90
	VC061-2.1	0.51	393	232	26	0.61	0.0539	2.2	0.569	2.4	0.0766	0.9	0.389	479.2	4.8	367	49	131
	VC061-3.1	0.76	252	138	17	0.56	0.0536	4.2	0.577	4.4	0.0780	1.3	0.300	489.6	6.7	354	94	138
	VC061-4.1	1.24	642	489	39.9	0.79	0.0617	4.0	0.608	4.3	0.0715	1.5	0.357	444.2	7.8	663	86	67
	VC061-5.1	0.87	375	268	24.6	0.74	0.0559	4.5	0.583	4.6	0.0757	1.0	0.215	470.5	5.0	447	99	105
	VC061-6.1	2.16	1105	1139	66.3	1.07	0.0565	5.3	0.533	5.4	0.0683	0.8	0.141	423.1	3.8	474	120	89
	VC061-7.1	0.36	522	304	36.4	0.60	0.0556	2.1	0.621	2.3	0.0810	0.8	0.360	506.7	4.5	436	48	116
	VC061-8.1	5.25	424	320	29.8	0.78	0.0487	14.0	0.521	14.0	0.0776	1.2	0.086	486.6	5.8	132	330	369
	VC061-9.1	2.46	87	14	5.63	0.17	0.0565	17.0	0.571	17.0	0.0733	2.3	0.132	455.8	9.3	470	380	97
	VC061-10.1	0.26	369	49	25.3	0.14	0.0572	2.8	0.628	3.0	0.0797	1.1	0.368	495.1	5.4	499	61	99
	VC061-11.1	2.09	943	444	60.9	0.49	0.057	5.3	0.578	5.4	0.0736	1.2	0.229	456.6	6.0	490	120	93
	VC061-12.1	0.38	539	450	35.8	0.86	0.0564	2.8	0.599	3.2	0.0771	1.6	0.498	483.8	8.6	468	62	103
	VC061-13.1	1.43	990	1313	66.7	1.37	0.0538	5.1	0.574	5.1	0.0773	0.7	0.134	489.1	3.8	364	110	134
	VC061-14.1	0.89	636	601	39.9	0.98	0.0579	3.5	0.577	3.6	0.0724	0.9	0.245	446	5.0	524	77	85
	VC061-15.1	--	175	25	12	0.15	0.0609	2.8	0.672	3.1	0.0800	1.4	0.440	495	6.7	635	60	78
VC123/1 Basalt	VC123-1-1.1	0.03	4657	438	189.0	0.10	0.05427	0.56	0.3534	1.2	0.04723	1.1	0.887	297.5	3.1	382	13	78
	VC123-1-2.1	--	1026	544	71.3	0.55	0.0578	0.87	0.6446	1.4	0.08088	1.1	0.789	501.4	5.4	522	19	96
	VC123-1-3.1	0.02	1974	1185	138.0	0.62	0.05706	0.68	0.6382	1.3	0.08112	1.1	0.850	502.8	5.3	494	15	102
	VC123-1-4.1	--	490	258	28.5	0.54	0.05559	1.60	0.5190	2	0.06775	1.2	0.590	422.6	4.8	436	36	97
	VC123-1-4.2	--	1044	685	72.9	0.68	0.05723	0.97	0.6421	1.5	0.08137	1.1	0.754	504.3	5.4	501	21	101
	VC123-1-5.1	0.04	1615	642	114.0	0.41	0.05678	0.76	0.6412	1.3	0.0819	1.1	0.824	507.5	5.4	483	17	105
	VC123-1-6.1	--	2144	991	151.0	0.48	0.05724	0.60	0.6473	1.2	0.08202	1.1	0.875	508.2	5.3	501	13	101
	VC123-1-7.1	--	1544	1208	108.0	0.81	0.05747	0.88	0.6439	1.4	0.08125	1.1	0.782	503.6	5.3	510	19	99
	VC123-1-8.1	0.04	2027	981	142.0	0.50	0.05697	0.79	0.6408	1.4	0.08157	1.1	0.810	505.5	5.3	491	17	103
	VC123-1-9.1	0.05	4847	3564	214.0	0.76	0.05502	0.59	0.3905	1.2	0.05148	1.1	0.879	323.6	3.4	413	13	78
	VC123-1-10.1	0.03	1575	1075	111.0	0.70	0.05696	0.74	0.6415	1.3	0.08169	1.1	0.832	506.2	5.4	490	16	103
	VC123-1-11.1	--	1324	842	92.3	0.66	0.05784	0.96	0.6484	1.5	0.0813	1.1	0.756	503.9	5.4	524	21	96

Continued

	Grain. spot	$^{206}Pb_c$ /%	Elem. content ($\times10^{-6}$) U	Th	$^{206}Pb^*$	$^{232}Th/^{238}U$	Radiogenic ratios $n(^{207}Pb)/n(^{206}Pb)$ Value	±/%	$n(^{207}Pb)/n(^{235}U)$ Value	±/%	$n(^{206}Pb)/n(^{238}U)$ Value	±/%	err corr.	Age/Ma $n(^{206}Pb)/n(^{238}U)$ Value	1σ	$n(^{207}Pb)/n(^{206}Pb)$ Value	1σ	Conc. /%
VC123/1 Basalt	VC123-1-12.1	--	723	371	52.7	0.53	0.0577	1.10	0.6760	1.5	0.08492	1.1	0.732	525.4	5.7	518	23	101
	VC123-1-13.1	0.04	1662	596	117.0	0.37	0.05683	0.74	0.6424	1.3	0.08199	1.1	0.831	508	5.4	485	16	105
	VC123-1-14.1	0.02	976	359	68.8	0.38	0.05733	0.93	0.6480	1.5	0.08197	1.1	0.769	507.9	5.5	504	21	101
	VC123-1-15.1	--	747	408	51.4	0.56	0.05726	1.20	0.6330	1.7	0.08012	1.2	0.690	496.8	5.5	502	27	99
VC123/3 Granitic Vein	VC123-3-1.1	0.12	208	97	37.2	0.48	0.0812	1.4	2.329	2.0	0.2079	1.5	0.726	1218.0	16	1227	27	99
	VC123-3-2.1	0.63	321	147	24.2	0.47	0.0577	3.4	0.693	3.6	0.0871	1.4	0.387	538.6	7.3	518	74	104
	VC123-3-2.2	1.23	314	139	22.3	0.46	0.0576	5.1	0.65	5.3	0.0818	1.3	0.240	506.6	6.2	516	110	98
	VC123-3-3.1	0.21	430	593	29.2	1.42	0.0555	1.7	0.603	2.0	0.0789	1.2	0.582	489.6	5.6	430	37	114
	VC123-3-4.1	5.39	470	135	36	0.30	0.0499	8.2	0.579	8.3	0.0843	1.3	0.153	521.5	6.3	189	190	276
	VC123-3-5.1	18.59	755	342	66.9	0.47	0.0500	36.0	0.58	36.0	0.0839	2.3	0.062	519.0	11	204	840	254
	VC123-3-6.1	0.19	429	162	29.7	0.39	0.0565	1.8	0.626	2.1	0.0804	1.2	0.558	498.6	5.7	471	39	106
	VC123-3-7.1	0.51	208	86	14.2	0.43	0.0552	5.1	0.6	5.3	0.0790	1.3	0.255	489.9	6.3	419	110	117
	VC123-3-8.1	0.31	385	328	26.4	0.88	0.0551	2.2	0.604	2.5	0.0795	1.2	0.489	493.4	5.7	417	48	118
	VC123-3-9.1	0.10	400	222	27.5	0.57	0.0567	1.7	0.625	2.2	0.0800	1.3	0.620	496.1	6.4	479	37	104
	VC123-3-10.1	--	150	16	10.1	0.11	0.0653	4.2	0.705	4.4	0.0783	1.5	0.334	486.2	6.9	784	88	62
	VC123-3-11.1	0.00	74	49	9.66	0.68	0.0719	2.9	1.499	3.3	0.1513	1.7	0.509	908.0	14	982	58	92

Notes: Pb_c and Pb* indicate the common and radiogenic portions, respectively; common Pb corrected using measured ^{204}Pb.

Most zircons from syenite sample VC008/1 have regular, long, columnar shapes, with grain length generally larger than 400 μm (Figure 5a). In CL images, the zircon grains are dark gray, with or without oscillatory zoning (Figure 5a). 14 zircons were analyzed from this sample with Th/U ratios of 0.52–0.81, indicating that these zircons are of magmatic origin (Belousova et al., 2002). The ages form a concordant cluster, giving a weighted mean $^{206}Pb/^{238}U$ age of 485.8 ± 5.7 Ma (Mean Standard Weighted Deviation (*MSWD*) = 0.93; Figure 6a). This age indicates that the syenite intruded during the Early Ordovician.

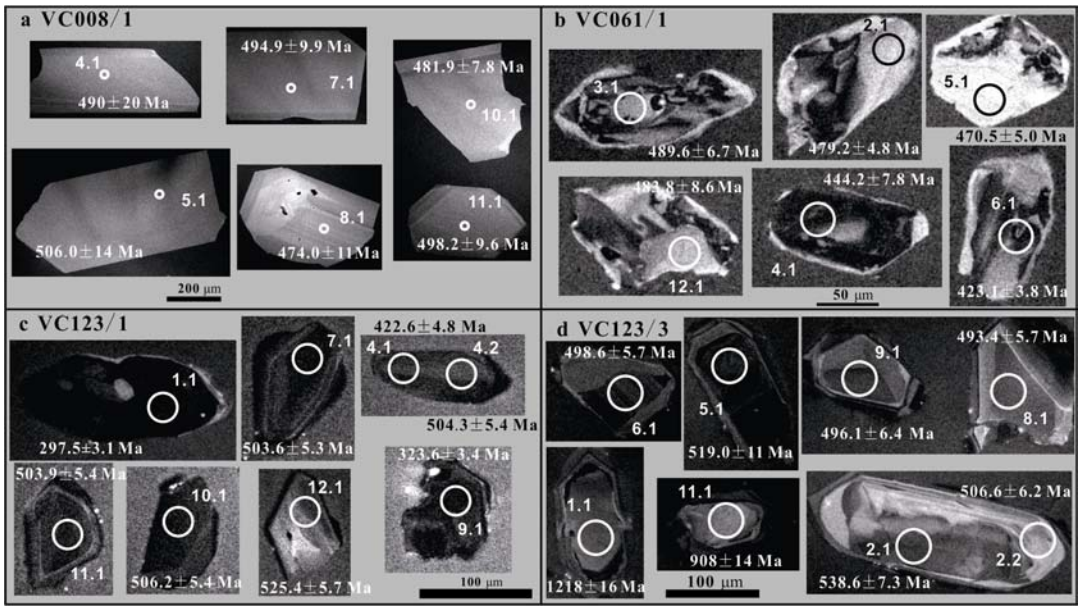

Figure 5 Representative CL images of zircons from the dated samples from Inexpressible Island. Also shown are the approximate positions, numbers and apparent $^{206}Pb/^{238}U$ ages (with 1σ) of the SHRIMP analytical spots (open circles outlined in white). **a**, Syenite from the eastern bay region. **b**, Monzodiorite intruded into the syenite. **c**, Basalt from the western alpine region. **d**, Granite vein intruded into basalt.

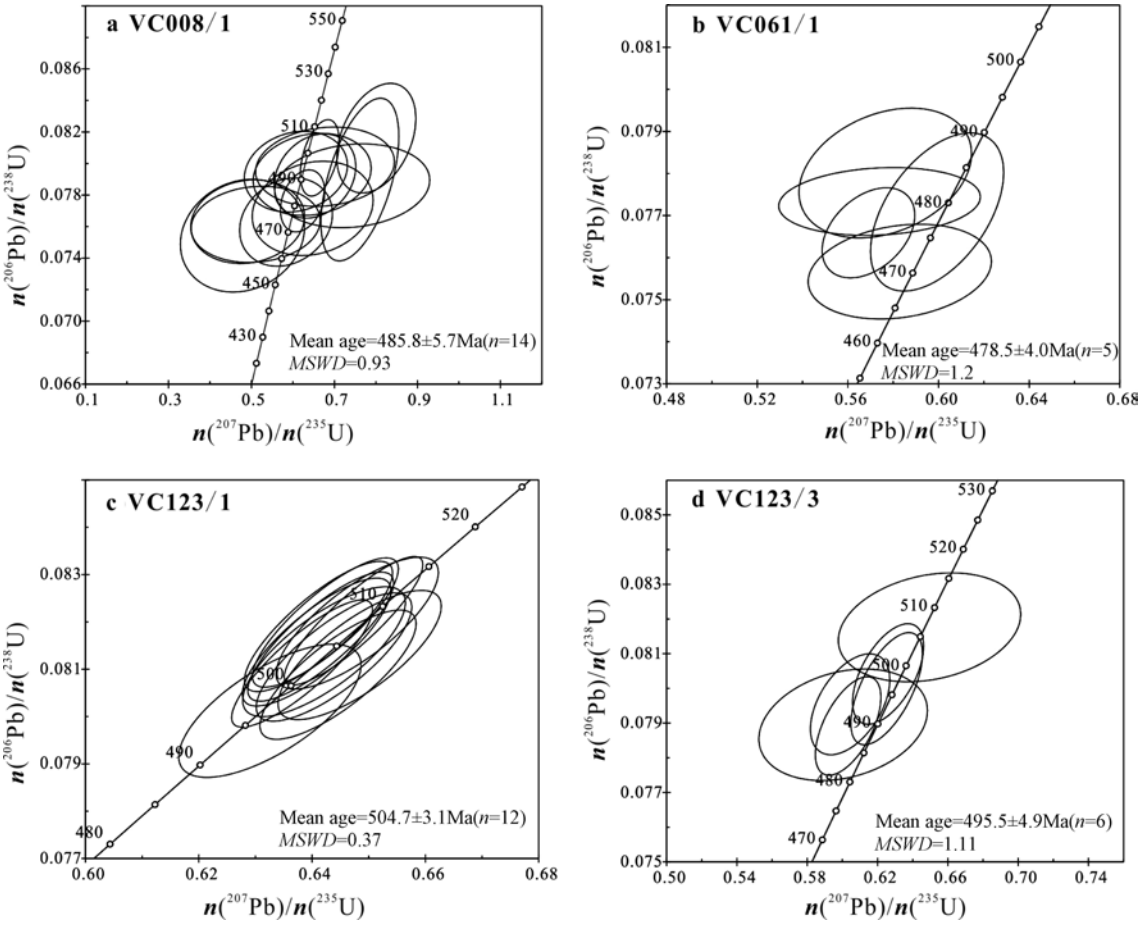

Figure 6 Concordia plots showing the SHRIMP zircon U–Pb data of Inexpressible Island in Northern Victoria Land. The error bars are 1σ. **a**, 14 samples of syenite from the eastern bay area. **b**, Five samples of monzodiorite intruded into the syenite. **c**, 12 samples of basalt from the western alpine region. **d**, Six samples from the granite vein intruded into basalt.

Zircons from monzodiorite vein VC61/1 are grayish white to grayish black, with length/width ratios of 1.0–2.0 and long-axis lengths of 100–150 μm. Some zircons have inherited cores (Figure 5b). 15 zircon spots were selected for dating. The Th/U ratios are all between 0.14 and 1.37, indicating a magmatic origin. The $^{206}Pb/^{238}U$ ages obtained for 10 zircon grains range from 507 to 470 Ma. Among them, five spots form a concordant cluster, with a weighted mean age of 478.5 ± 4.0 Ma (*MSWD*=1.2; Figure 6b). This age indicates magma intrusion during the Early Ordovician. Spots 4.1, 6.1, 9.1, 11.1, and 14.1 have high U contents and yield $^{206}Pb/^{238}U$ ages younger than 478.5 ± 4.0 Ma, likely representing the timing of late hydrothermal activity (Table 2; Figure 5b).

Zircons from basalt sample VC123/1 are mostly gray to black euhedral columnar crystals with length/width ratios of 1.0–2.0. The long axes range from 100 to 150 μm in length. These zircons exhibit well-developed oscillatory zoning (Figure 5c). A total of 16 spots were dated, of which 12 form an age cluster, excluding spots 1.1, 4.1, 9.1, and 12.1. Th/U ratios are between 0.41 and 0.81, indicating a magmatic origin. Ten clustered $^{206}Pb/^{238}U$ ages range from 496 to 508 Ma, giving a weighted mean age of 504.7 ± 3.1 Ma (*MSWD* = 0.37; Figure 6c). This age implies magma eruption during the late Cambrian. The $^{206}Pb/^{238}U$ ages of spots 1.1, 4.1, and 9.1 are 297.5, 422.6, and 323.6 Ma, respectively. Spots 1.1 and 9.1 are from dark zircon grains with high U content, which may indicate younger hydrothermal activity (Table 2). The $^{206}Pb/^{238}U$ age of spot 12.1 is 525.4 Ma, which may represent an inherited zircon age.

Zircons from granite vein VC123/3 are mostly gray to black, euhedral columnar crystals with lengths of 120 to 180 μm and length/width ratios of 1.0–2.0. Most zircon grains display well-developed oscillatory zoning, and some have an inherited core (Figure 5d). The Th/U ratios of the 12 zircon spots selected for dating are between 0.11 and 1.42, indicating a magmatic origin. Excluding spots 1.1 and 11.1, the other 10 spots yield clustered $^{206}Pb/^{238}U$ ages between 538–486 Ma. The weighted mean age calculated based on the six spots is 495.5 ± 4.9 Ma (*MSWD* = 1.11; Figure 6d). The $^{206}Pb/^{238}U$ ages of spots 1.1 and 11.1 are 1218 and 908 Ma, respectively, corresponding to the ages of inherited cores from the Proterozoic basement (Figure 5d). The ages measured in the core and mantle of zircon 2.1 are 538 and 506 Ma, respectively. The core age represents an inherited zircon age, whereas the mantle age corresponds closely with the intrusive age of the late Cambrian vein.

Table 3 Major- and trace-element compositions of selected samples from Inexpressible Island

	Sample	Syenite									Monzodiorite					Basalt			
		VC008/1	VC011/2	VC048/1	VC049/2	VC051/1	VC053/1	VC055/1	VC059/1	VC060/1	VC061/1	VC061/2	VC061/3	VC061/4	VC061/5	VC123/1	VC123/2	VC123/3	VC123/4
Major elements /(wt.%)	SiO_2	62.09	62.25	62.86	62.48	62.19	61.35	62.59	62.48	61.33	55.35	58.35	55.32	55.81	55.88	40.89	46.85	46.99	47.16
	TiO_2	0.52	0.52	0.48	0.46	0.55	0.65	0.58	0.59	0.58	1.92	1.62	1.93	1.93	2.02	0.44	0.56	0.49	0.54
	Al_2O_3	17.56	17.82	17.87	18.25	17.49	17.42	17.88	17.99	17.85	15.42	14.90	15.48	15.47	15.72	9.06	10.03	9.62	10.08
	Fe_2O_{3T}	4.92	5.24	4.47	4.33	5.38	6.17	4.65	4.43	5.61	8.92	7.69	8.92	8.98	9.41	9.76	11.39	11.81	11.32
	MnO	0.10	0.14	0.09	0.09	0.12	0.12	0.10	0.10	0.12	0.14	0.11	0.13	0.13	0.13	0.16	0.18	0.19	0.18
	MgO	0.41	0.43	0.36	0.39	0.44	0.51	0.56	0.58	0.49	3.57	3.54	3.54	3.55	3.46	14.65	17.08	17.42	16.84
	CaO	2.24	1.87	1.90	2.11	2.31	2.40	2.17	2.30	2.68	6.36	5.11	6.29	6.37	6.32	7.98	9.02	9.47	9.93
	Na_2O	3.16	3.11	3.12	3.31	2.78	3.01	3.16	2.95	3.12	3.13	2.89	2.90	3.03	3.00	0.75	0.88	0.81	0.86
	K_2O	7.99	7.97	8.03	8.10	7.84	7.88	7.62	7.57	7.37	3.05	3.86	3.54	3.36	2.77	0.88	0.93	0.86	1.13
	P_2O_5	0.13	0.16	0.11	0.11	0.12	0.14	0.15	0.16	0.14	0.86	0.71	0.86	0.85	0.90	0.09	0.12	0.10	0.11
	LOI	0.33	0.41	0.43	0.41	0.47	0.27	0.30	0.55	0.20	0.60	0.67	0.58	0.57	0.46	14.82	2.67	2.19	1.56
	Total	99.45	99.91	99.72	100.03	99.67	99.92	99.75	99.70	99.47	99.32	99.45	99.48	100.05	100.08	99.50	99.72	99.95	99.70
	Na_2O+K_2O	11.15	11.08	11.14	11.41	10.61	10.88	10.78	10.52	10.49	6.18	6.75	6.44	6.39	5.77	1.64	1.81	1.67	1.99
K_2O/Na_2O		2.53	2.56	2.58	2.44	2.82	2.62	2.41	2.57	2.36	0.97	1.34	1.22	1.11	0.92	1.17	1.06	1.07	1.31
AR		3.58	3.58	3.58	3.55	3.31	3.43	3.33	3.15	3.09	1.79	2.02	1.84	1.83	1.71	1.21	1.21	1.19	1.22
A/CNK		0.98	1.04	1.03	1.01	1.01	0.98	1.03	1.04	0.99	0.77	0.82	0.77	0.77	0.81	0.54	0.53	0.49	0.49
A/NK		1.27	1.30	1.29	1.28	1.34	1.29	1.33	1.38	1.36	1.82	1.67	1.80	1.80	1.98	4.13	4.08	4.25	3.82
$Mg^{\#}$		0.039	0.049	0.127	0.127	0.165	0.189	0.170	0.157	0.171	0.615	0.556	0.440	0.478	0.421	0.748	0.748	0.745	0.747
Rittmann Index (σ)		6.51	6.38	6.25	6.69	5.87	6.45	5.93	5.68	6.01	3.09	2.97	3.36	3.19	2.59	--	0.85	0.70	0.95
Trace elements /($\mu g \cdot g^{-1}$)	Sc	24.09	17.6	17.73	16.82	26.3	30.6	16.88	18.76	27.03	17.13	14.42	17.33	17.2	15.17	29.08	30.15	29.11	28.62
	V	4.159	4.605	4.392	3.187	5.788	6.183	4.994	7.598	4.269	93.95	77.87	94.16	94.28	95.41	130.6	142.2	112.8	132.9
	Cr	1.693	1.789	2.064	1.649	1.977	2.255	4.007	4.257	3.084	54.86	84.94	41.14	47.32	39.99	1122.8	1156.4	1150.4	1094.4
	Co	1.485	1.549	1.676	1.407	1.692	1.915	2.085	2.237	2.027	19.4	17.88	20.77	20.29	20.22	65.4	69.22	67.52	62.59
	Ni	0.845	0.798	1.26	1.131	1.021	1.238	1.073	1.204	1.368	18.64	24.67	17.87	18.06	15.09	209.2	230.5	227.1	202.1
	Cu	3.561	2.937	4.014	3.59	3.803	7.5	3.785	3.71	6.378	11.59	12.01	13.02	27.78	13.09	43.02	49.79	49.86	58.46
	Sc	24.09	17.6	17.73	16.82	26.3	30.6	16.88	18.76	27.03	17.13	14.42	17.33	17.2	15.17	29.08	30.15	29.11	28.62
	V	4.159	4.605	4.392	3.187	5.788	6.183	4.994	7.598	4.269	93.95	77.87	94.16	94.28	95.41	130.6	142.2	112.8	132.9
	Cr	1.693	1.789	2.064	1.649	1.977	2.255	4.007	4.257	3.084	54.86	84.94	41.14	47.32	39.99	1122.8	1156.4	1150.4	1094.4
	Co	1.485	1.549	1.676	1.407	1.692	1.915	2.085	2.237	2.027	19.4	17.88	20.77	20.29	20.22	65.4	69.22	67.52	62.59
	Ni	0.845	0.798	1.26	1.131	1.021	1.238	1.073	1.204	1.368	18.64	24.67	17.87	18.06	15.09	209.2	230.5	227.1	202.1
	Cu	3.561	2.937	4.014	3.59	3.803	7.5	3.785	3.71	6.378	11.59	12.01	13.02	27.78	13.09	43.02	49.79	49.86	58.46
	Zn	65.03	80	72.86	67.21	83.44	86.3	79.83	59.38	63.5	133.9	116.1	139.6	137.9	140.1	99.97	90.55	90.5	89.82
	Ga	17.91	18.25	19.1	18.19	18.74	18.53	19.06	17.84	17.91	23.24	21.52	23.63	23.22	23.61	11.36	11.16	10.62	11.01
	Rb	155	212.2	225.3	166.2	206.7	167.7	210	199.5	167.6	234.3	169	228.5	218.9	198.6	46.18	39.91	38.16	55.88

Continued

	Sample	Syenite									Monzodiorite					Basalt			
		VC008/1	VC011/2	VC048/1	VC049/2	VC051/1	VC053/1	VC055/1	VC059/1	VC060/1	VC061/1	VC061/2	VC061/3	VC061/4	VC061/5	VC123/1	VC123/2	VC123/3	VC123/4
Trace elements /(μg·g^{-1})	Sr	297	276.8	286.4	295.7	286.7	279.2	309	360.2	332	506.1	479.6	579.3	558.5	605.9	244.3	221.5	190.5	198.8
	Y	11.16	8.153	9.267	10.44	13.52	11.65	10.97	10.01	11.92	45	36.87	44.82	45.91	42.3	12.59	14.11	12.75	12.76
	Zr	214.9	175.6	274.2	74.29	104.6	273.2	219.2	160	69.63	526	342.8	527.6	495.8	158.7	60.55	63.87	59.46	58.97
	Nb	8.685	11.36	8.462	8.784	9.237	10.5	19.21	10.58	12.67	37.37	27.47	36.51	36.74	36.47	3.532	4.081	3.387	3.622
	Cs	3.208	21.01	23.33	9.573	16.66	7.222	10.97	5.131	6.307	11.57	7.088	8.616	9.964	8.904	8.318	7.743	8.077	17.4
	Ba	4151.9	3574	4120.2	4152.5	4115	3884.9	3766.5	4931.9	4611.8	1239.3	957.8	1275.6	1185.4	1196.7	205.3	168.1	179	225.7
	Hf	4.467	3.53	5.056	1.912	2.526	5.219	4.216	3.326	1.723	11.94	8.074	11.86	11.01	3.88	1.795	1.912	1.778	1.758
	Ta	0.577	0.871	0.612	0.567	0.777	0.756	1.32	0.847	1.2	2.116	1.819	1.975	2.038	1.945	0.237	0.258	0.22	0.232
	Pb	15.33	20.83	20.24	20.09	20.1	17.17	24.08	23.85	22.21	18.84	20.61	20.89	18.19	17.9	2.864	3.033	2.712	2.419
	Th	4.103	6.595	4.071	6.116	5.345	4.609	8.44	4.525	2.153	9.784	11.57	9.545	10.15	9.1	1.895	2.706	1.939	1.943
	U	0.543	1.282	0.666	0.89	1.126	0.696	0.681	1.011	0.96	2.788	4.799	2.343	2.932	2.168	0.438	0.492	0.453	0.477
	Ge	1.797	1.766	1.619	1.636	1.944	1.908	1.719	1.481	1.825	3.71	3.105	3.644	3.673	3.794	2.628	2.647	2.73	2.645
	Ti	3094.5	3057.8	2761.6	2624.7	3242.3	3813.1	3670.5	3592.8	3672.6	11467.5	9746.3	11665.2	11498.3	11741.1	3019.4	3326	2820.1	3117.6
	Mn	779.8	1042.8	727	678.4	899.7	955.5	755.6	785.4	930.4	1059	883.3	1027.6	992.2	997.4	1469.8	1395.6	1451.6	1375.3
	La	19.56	13.23	13	15.92	26.54	16.13	26.79	14.53	12.48	91.24	68.92	95.42	90.19	90.92	10.29	10.73	9.854	9.846
	Ce	38.49	22.87	26.63	33.18	54.69	35.33	54.18	29.31	27.68	188.9	140.4	193.9	180.1	187.1	23.18	24.94	22.44	22.53
	Pr	4.566	2.345	3.238	4.037	6.524	4.575	6.34	3.429	3.663	22.92	17.58	23.27	22.2	23.14	3.043	3.375	2.974	3.058
	Nd	18.02	9.045	13.03	15.61	24.59	19.15	23.12	13.68	15.3	88.03	68.52	89.4	87.93	87.82	12.84	14.73	13.07	13.07
	Sm	3.324	1.844	2.486	3.066	4.427	3.809	4.238	2.652	3.418	15.57	12.37	15.46	15.39	15.55	2.813	3.244	2.842	2.917
	Eu	4.188	3.636	3.946	3.984	4.131	4.303	3.36	4.194	4.305	3.096	2.352	3.026	2.901	3.13	0.79	0.847	0.79	0.84
	Gd	2.91	1.884	2.15	2.661	3.673	3.22	3.517	2.466	3.019	12.5	9.986	12.69	12.61	12.46	2.607	2.995	2.654	2.653
	Tb	0.404	0.279	0.312	0.363	0.523	0.474	0.472	0.355	0.457	1.768	1.411	1.727	1.692	1.694	0.417	0.478	0.43	0.435
	Dy	2.196	1.58	1.754	2.093	2.75	2.482	2.317	1.947	2.417	9.149	7.477	8.944	9.008	8.769	2.463	2.791	2.449	2.499
	Ho	0.442	0.314	0.361	0.393	0.542	0.481	0.441	0.396	0.46	1.743	1.441	1.756	1.751	1.693	0.499	0.564	0.505	0.51
	Er	1.202	0.854	0.975	1.054	1.388	1.212	1.092	1.038	1.179	4.598	3.68	4.403	4.45	4.262	1.286	1.465	1.337	1.326
	Tm	0.169	0.119	0.139	0.152	0.194	0.168	0.152	0.144	0.161	0.62	0.499	0.62	0.602	0.563	0.18	0.203	0.189	0.189
	Yb	1.169	0.818	0.921	0.923	1.249	1.073	0.96	0.929	1.043	3.911	3.118	3.871	3.799	3.509	1.135	1.264	1.17	1.15
	Lu	0.193	0.136	0.16	0.153	0.196	0.179	0.155	0.145	0.162	0.588	0.462	0.573	0.584	0.533	0.171	0.194	0.178	0.179
	∑REE	96.83	58.95	69.10	83.59	131.42	92.59	127.13	75.22	75.74	444.63	338.22	455.06	433.21	441.14	61.71	67.82	60.88	61.20
La/Lu		101.35	97.28	81.25	104.05	135.41	90.11	172.84	100.21	77.04	155.17	149.18	166.53	154.43	170.58	60.18	55.31	55.36	55.01
LREE/HREE		10.15	8.85	9.20	9.73	11.50	8.97	12.96	9.14	7.51	11.75	11.05	12.16	11.56	12.18	6.05	5.81	5.83	5.85
$(La/Yb)_N$		11.28	10.90	9.52	11.63	14.33	10.13	18.81	10.54	8.07	15.73	14.90	16.62	16.01	17.47	6.11	5.72	5.68	5.77
$(Gd/Yb)_N$		2.01	1.86	1.88	2.33	2.37	2.42	2.96	2.14	2.34	2.58	2.58	2.65	2.68	2.87	1.85	1.91	1.83	1.86
δEu		3.34	4.95	4.22	3.45	2.51	3.03	2.14	4.10	3.33	0.54	0.52	0.53	0.51	0.55	0.73	0.68	0.72	0.75

5 Geochemical characteristics

Eighteen samples were selected for geochemical study, comprising nine syenite samples, five monzodiorite samples, and four basalt samples (Table 3). The specific sampling locations are shown in Figure 1.

All the samples for the geochemical study were separated from their weathering crusts, crushed in a hardened jaw crusher, and then powdered in an agate mill to a grain size smaller than 200 mesh. The samples were tested in a laboratory at Guangzhou Geochemistry Institute of the Chinese Academy of Sciences in Guangzhou, China. The major-element analyses of the whole-rock samples were performed using a Rigaku RIX2000 X-ray fluorescence spectrometer. Fe_2O_{3T} represents the total amount of FeO and Fe_2O_3. The methods used were the same as those described by Li (1997). The element composition of the samples was determined using a working curve obtained via bivariate fitting of 36 reference standards covering the range of silicate samples. Matrix correction was conducted using the experimental Traill Lachance program, with an analytical accuracy of 1%–5% (Li, 1997). Trace-element analyses were conducted using a Perkin Elmer Sciex Elan6000 ICP–MS. The procedure used was the same as that described by Li et al. (2005). The United States Geological Survey standards W2 and BHVO-2 and Chinese national standards GSR-1, GSR-2, and GSR-3 were used to correct the element compositions of the samples. The analytical accuracy was generally 2%–5%. The results for all samples are listed in Table 3.

5.1 Major elements

The nine syenite samples have SiO_2 contents of 61.33–62.86 wt.%, Na_2O contents of 2.78–3.31 wt.%, and K_2O contents of 7.37–8.1 wt.%. The total alkali contents are 10.49–11.41 wt.%, with K_2O/Na_2O ratios of 2.36–2.82, alkalinity ratio (AR) values of 3.09–3.58, and Rittmann index (σ) values of 5.68–6.69, which is indicative of alkaline rocks. All the samples fall in the syenite area on a total alkali versus silica (TAS) diagram and belong to the alkaline series (Figure 7a). The contents of Al_2O_3 vary between 17.42 and 18.25 wt.%. The CaO contents are as high as 1.87–2.68 wt.%. The A/CNK values are between 0.98 and 1.04, and the A/NK values are 1.27–1.38, which imply quasi-aluminous to peraluminous characteristics. MgO contents are 0.36–0.58 wt.%, and Mg# values are between 0.039 and 0.189.

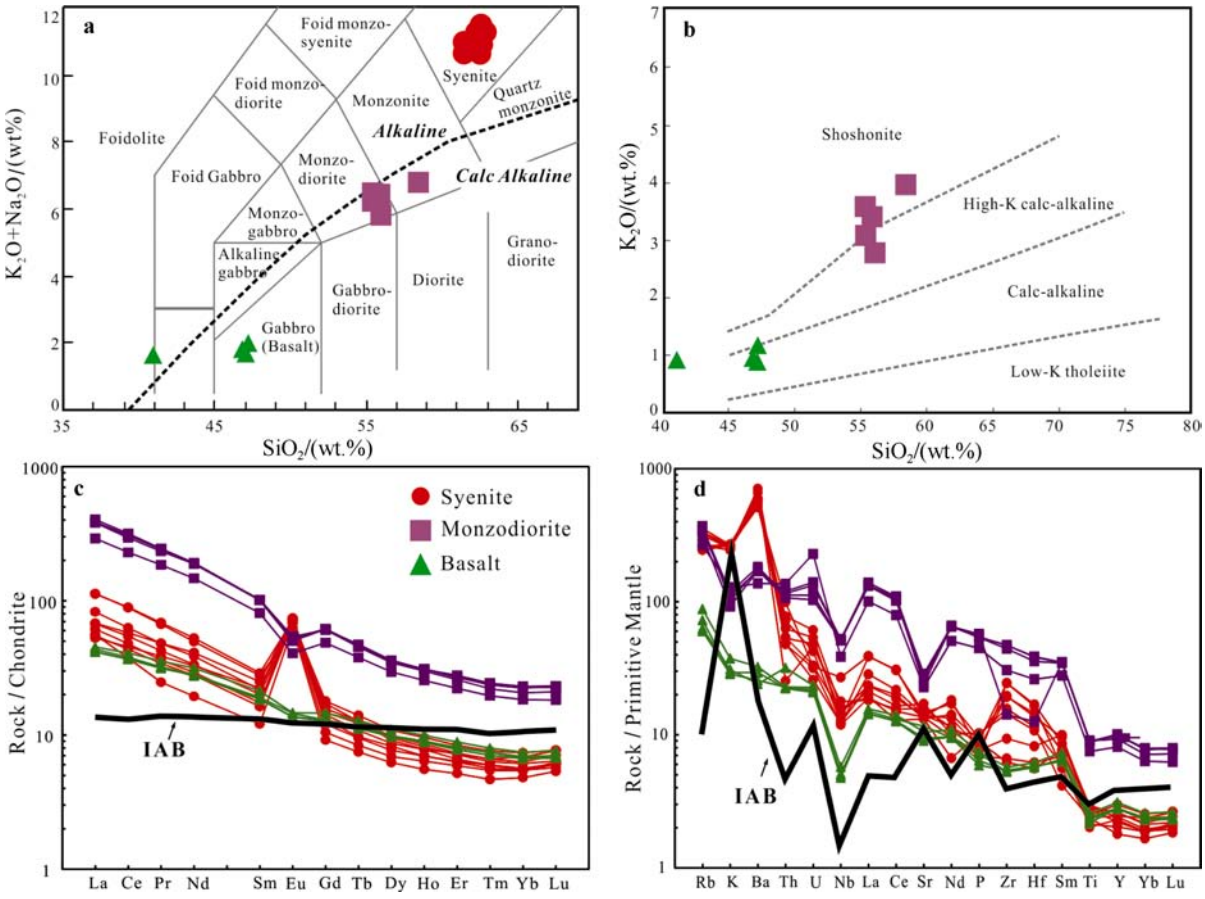

Figure 7 Geochemical analysis diagrams of the magmatic rocks. **a**, Alkali–silica diagram (Middlemost, 1994); **b**, SiO_2–K_2O for rock classification diagram (Peccerillo and Taylor, 1976); **c**, Chondrite-normalized REE distribution patterns; **d**, plots of primitive-mantle-normalized trace-element patterns. The data for island-arc basalt (IAB) are from Yang et al. (2016).

The five monzodiorite samples have SiO_2 contents of 55.32–58.35 wt.%, Na_2O contents of 2.89–3.13 wt.%, and K_2O contents of 2.77–3.86 wt.%, indicative of intermediate rocks. The total alkali contents are 5.77–6.75 wt.%, with K_2O/Na_2O ratios of 0.92–1.34, AR of 1.71–2.02, and σ of 2.59–3.36, which is characteristic of calc-alkaline rocks (Figure 7a). All of these samples plot within the monzodiorite and monzonite region on a TAS diagram and belong to the calc-alkaline series (Figure 7a). They also belong to the shoshonite–high-K calc-alkaline series in a K_2O–SiO_2 diagram (Figure 7b). The Al_2O_3 contents are 14.9–15.72 wt.%, and the CaO contents are 5.11–6.37 wt.%. The A/CNK values are 0.77–0.82, and the A/NK values are 1.67–1.98, which indicates quasi-aluminous characteristics. The MgO contents are 3.46–3.57 wt.%, and Mg# values are between 0.421 and 0.615.

The four basalt samples have low SiO_2 contents of 40.89–47.16 wt.%, Na_2O contents of 0.75–0.88 wt.%, and K_2O contents of 0.86–1.13 wt.%. The total alkali contents are 1.64–1.99 wt.%, with K_2O/Na_2O ratios of 1.06–1.31, AR of 1.19–1.22, and σ of 0.7–0.95, which is indicative of calc-alkaline rocks (Figure 7b). Most of the samples plot within the gabbro (basalt) region on a TAS diagram and belong to the calc-alkaline series on a K_2O–SiO_2 diagram, except for sample VC123/1 (Figures 7a–b). The Al_2O_3 contents are 9.06–10.08 wt.%, and the CaO contents are 7.98–9.93 wt.%. The A/CNK values are 0.49–0.54, and the A/NK values lie between 3.82 and 4.25, indicating quasi-aluminous characteristics. The MgO contents are 14.65–17.42 wt.%, and Mg# values are between 0.745 and 0.748.

5.2 Trace elements

The total concentration of rare-earth elements (REEs) in the syenite samples varies between 58.95 and 131.42 $\mu g \cdot g^{-1}$. Light REEs (LREEs) are highly enriched, and heavy REEs (HREEs) are depleted, with $(La/Yb)_N$ ratios of 8.07–18.81 and $(Gd/Yb)_N$ ratios of 1.86–2.96 (Figure 7c). All samples show positive Eu anomalies, with δEu = 2.14–4.95.

The total concentration of REEs in the monzodiorite samples ranges from 338.22 to 455.06 $\mu g \cdot g^{-1}$. LREEs are highly enriched, and HREEs are depleted, with $(La/Yb)_N$ ratios of 14.9–17.47 and $(Gd/Yb)_N$ ratios of 2.58–2.87 (Figure 7c). All samples show negative Eu anomalies, with δEu = 0.51–0.55.

The total concentration of REEs in the basalt samples ranges from 60.88 to 67.82 $\mu g \cdot g^{-1}$. LREEs are highly enriched, and HREEs are mildly depleted, with $(La/Yb)_N$ ratios of 5.68–6.11 and $(Gd/Yb)_N$ ratios of 1.83–1.91 (Figure 7c). All samples show negative Eu anomalies, with δEu = 0.68–0.75.

In the primitive-mantle-normalized trace-element spider diagram (Figure 7d), all the syenites are depleted in high-field-strength elements (HFSEs), such as K, Nb, P, and Ti, and are enriched in large-ion lithophile elements (LILEs), such as Ba, Rb, and Zr. The monzodiorites are depleted in HFSEs, such as K, Nb, Sr, and Ti, and are enriched in LILEs, such as Rb, Nd, and Sm. The distribution curves in the spider diagram of the basalt samples are similar to those of the monzodiorites.

6 Discussion

Our regional investigation showed that the Terra Nova Intrusive Complex of Northern Victoria Land was a good indicator of the development of the Ross Orogen (Vincenzo and Rocchi, 1999; Federico et al., 2009; Rocchi et al., 1998, 2015). Here, we further define the relationship between the Abbott Unit and the Vegetation Unit magma series in the Terra Nova Complex based on lithological, geochronological, and geochemical studies.

6.1 Sequence of magmatism

The field investigation indicated that the magmatic activity in southern Inexpressible Island produced mainly syenite and basalt, with the late-stage development of a large number of granitic and mafic veins (Figure 3). Previous studies concluded that this basalt series belonged to the Vegetation Unit and that the large areas of syenite and various late-stage veins indicated that the magmatic activity in the extensional setting developed during the later stages of Ross Orogeny (Vincenzo and Rocchi, 1999). The results of the present study date the formation of the basalt exposed in the alpine region of western Inexpressible Island to 504.7 ± 3.1 Ma and a vein of granite to 495.5 ± 4.9 Ma. These zircon U–Pb dating results are in good agreement with the intrusion sequences observed in the field (Figure 3h). The contact relationship between the basalt and syenite was not observed in the field because of snow cover. Our SHRIMP zircon U–Pb dating gave an emplacement age of the syenite of 485.8 ± 5.7 Ma, which matches the previous ages determined using LA–ICP–MS (Wang et al., 2014). The SHRIMP zircon U–Pb age of the monzodiorite intruded into this syenite series is 478.5 ± 4.0 Ma, which is consistent with the intrusion sequence determined in the field (Figure 3f). The field investigation revealed a large number of granitic veins in the syenite and mafic veins in the basalt (Figure 3). Previous studies have defined these mafic and granitic veins as being produced in the same tectonic setting (Rocchi et al., 1998; Vincenzo and Rocchi, 1999). However, the present geochronological determinations reveal that the intrusion ages of these two sets of veins are significantly different, which are 478.5 ± 4.0 Ma and 495.5 ± 4.9 Ma respectively. Considering both the field observations of the intrusion sequence and the dating results, we infer that the Terra Nova Intrusive Complex underwent two stages of magmatic activity. The earlier stage consisted of basalt-dominated volcanism with subsequent intrusions of mafic and acidic veins at middle to late Cambrian, and the later stage involved magmatic intrusions dominated by syenite that were intruded by both mafic and acidic veins at Early Ordovician.

6.2 Tectonic setting of magmatic activity

We deduced the tectonic location of the southwestward subduction of the paleo-Pacific plate from the geochemical differences between the studied rocks. The Terra Nova Intrusive Complex was located on the continental side of the subduction zone during the Cambrian–Ordovician (Rocchi et al., 1998; Federico et al., 2009). Recent research indicates two stages of magmatic activity during the initiation of the Ross subduction, at ~521 and 510–490 Ma, with different magma sources in the Teall Nunatak area in the western part of Inexpressible Island (Giacomini et al., 2007). The intrusions associated with the younger magmatic events were related to the initial subduction of the ocean basin (Giacomini et al., 2007). The Terra Nova Intrusive Complex, which includes Inexpressible Island, presents a record of the subduction and collision of the Ross Orogen (Rocchi et al., 1998; Vincenzo and Rocchi, 1999). However, because previous studies focused mainly on early (Cambrian) subduction and collision processes in this area (Black and Sheraton, 1990; Vincenzo and Rocchi, 1999; Federico et al., 2009), less attention has been paid to the later (Ordovician) magmatic evolution and tectonic setting.

Our field mapping and zircon dating reveal that there were two stages of magmatic activity in the Terra Nova Intrusive Complex during 504.7–495.5 Ma and 485.8–478.0 Ma respectively. Geochemical analyses of three major rock types—basalt, syenite, and monzodiorite—show clear distinctions in major elements. The total amounts of REEs in the monzodiorite are significantly higher than those in the syenite and basalt. The Eu anomalies found in the syenite also differ from those in the other two rock types. Trace-element analysis indicates depletion in HFSEs (K, Nb, and Ti) in all three rock types and enrichment in LILEs (e.g., Rb). The Ba and Zr contents of the basalt differ considerably from those in the other two rock types. All of these features indicate three types tectonic settings for each rock (Figure 7).

Few studies have discussed the tectonic setting of the late-stage syenite. A tectonic setting discrimination diagram of the major and trace elements reveals that the syenite lies between A-type and I–S-type granite, showing transitional properties between these two types (Figure 8a). In the Rb–Y+Nb and R1–R2 diagrams, the syenite is classified as syn-collisional granite and post-orogenic granite, respectively (Figure 8b–8c). These results indicate a post-orogenic collisional setting for the emplacement of these rocks during the Early Ordovician and a tectonic transition from collision to extension.

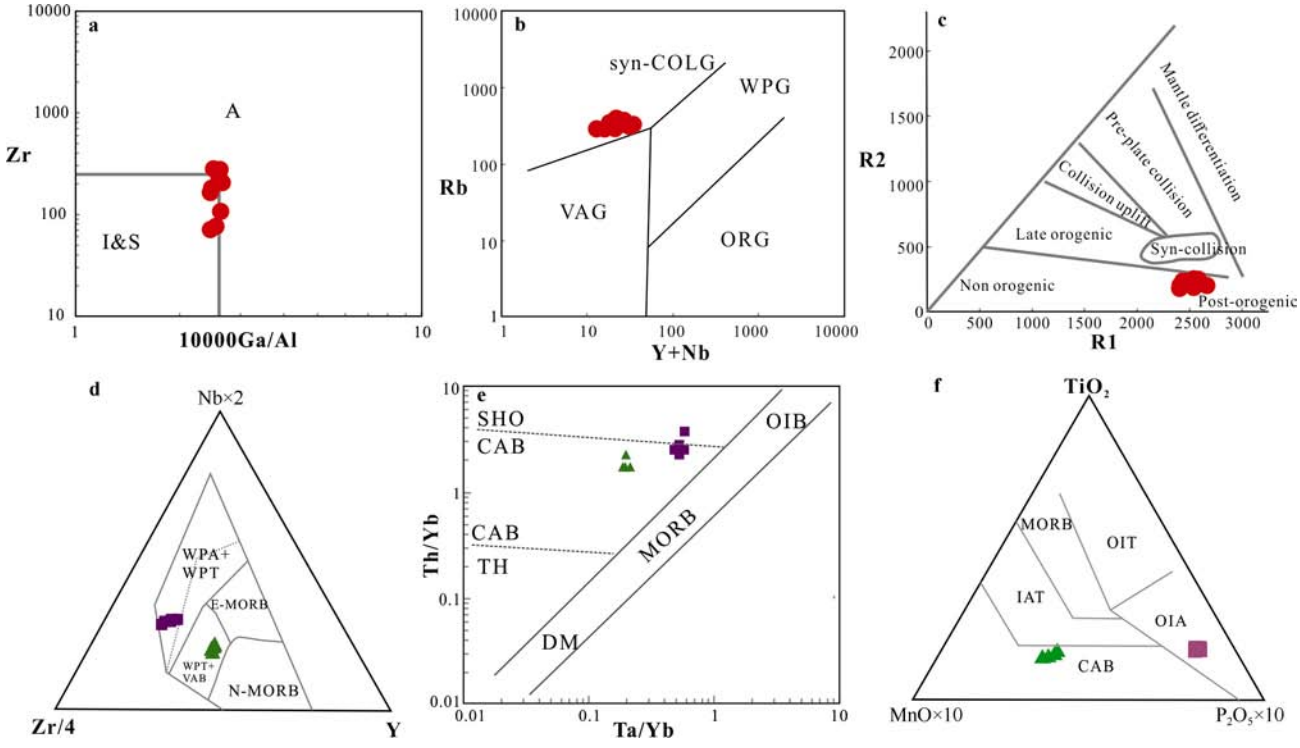

Figure 8 Tectonic setting discrimination diagrams for trace elements in the magmatic rocks. The sample legend is the same as in Figure 7. **a**, Zr–10000 Ga/Al; **b**, Rb–Y+Nb; **c**, R2–R1; **d**, Nb×2–Zr/4–Y; **e**, Th/Yb–Ta/Yb; **f**, TiO_2–MnO×10–P_2O_5×10. A: A-type granite; CAB: continental arc basalt; DM: depleted mantle; E-MORB: E-type MORB; I: I-type granite; IAT: island-arc tholeiite; MORB: mid-ocean ridge basalt; N-MORB: N-type MORB; OIA: ocean island alkaline basalt; OIB: ocean island basalt; OIT: ocean island tholeiite; ORG: ocean ridge granite; S: S-type granite; SHO: shoshonite; syn-COLG: syn-collisional granite; TH: tholeiite; VAB: volcanic arc basalt; VAG: volcanic arc granite; WPA: within-plate alkaline basalt; WPG: within-plate granite; WPT: within-plate tholeiite.

The tectonic settings of the basalt and the monzodiorite veins, which formed before and after the syenite, respectively, differ from that of the syenite. In the Nb×2–Zr/4–Y, Th/Yb–Ta/Yb, and TiO_2–MnO×10–P_2O_5×10 discrimination diagrams, the monzodiorite falls into the within-plate or ocean island basalt fields, which represent an extensional environment (Figures 8d–8f). However, the basalt falls mainly within the volcanic arc region (Figures 8d–8f), which indicates an island-arc setting. The arc-related granitoid rocks and granites are developed in the northern Terra Nova Intrusive Complex (Rocchi et al., 1998). The Abbott Unit in the Terra Nova Intrusive Complex is also composed of felsic, mafic, and intermediate facies rocks, including granite (Vincenzo and Rocchi, 1999). These compositional and age characteristics are generally consistent with those of Southern Victoria Land, which formed within a continental arc (Hagen-Peter and Cottle, 2016). Although there are some differences between the basalt samples and IAB in the chondrite-normalized REE distribution patterns and primitive-mantle-normalized trace-element patterns (Figures 7c–7d), the basalts fall in the continental arc basalt (CAB) setting field (Figures 8e–8f). This may be related to the continental-margin setting in which these basalts formed (Rocchi et al., 1998). In addition, the K_2O, Na_2O, TiO_2, Nb, Ta, and Pb contents of the basalts are clearly lower than those of the other rocks (Table 3). Therefore, our new geochemical data imply that the basalt was formed in a continental-margin arc setting and that the monzodiorite was formed in an extensional setting. These results are consistent with the findings of previous studies (Rocchi et al., 1998; Vincenzo and Rocchi, 1999).

6.3 Tectonic evolution

By identifying the multiple stages of magmatic activity and the different tectonic settings of Inexpressible Island rocks, we are able to reconstruct the magmatic and tectonic evolution of the area during the middle Cambrian and Early Ordovician. Eclogite-facies metamorphism in Northern Victoria Land is dated as early as ~530 Ma, which together with geochronological evidence for the emplacement of calc-alkaline granitoids at ~530–520 Ma suggests the existence of an active continental margin during this stage (Godard and Palmeri, 2013; Di Vincenzo et al., 2016; Merdith et al., 2017). During the middle Cambrian (~505 Ma), the paleo-Pacific plate subducted toward the Wilson Terrane of East Antarctica, forming a magmatic arc near the subduction zone and producing numerous mafic volcanic rocks, intrusive rocks, and late-stage granite veins (Federico et al., 2009; Rocchi et al., 2015; Hagen-Peter and Cottle, 2016). After ~20 Ma of subduction, the Ross Orogen entered a later stage of orogeny during the Early Ordovician. This post-orogenic collision gave rise to voluminous syenite (Rocchi et al., 2015). This stage also involved the transition of tectonic conditions in the entire Ross Orogen from collisional to extensional, with the subsequent onset of intracontinental extension. At the same time, mafic veins with continental tholeiitic properties were formed. Our results therefore constrain the complete evolution of the Ross Orogen from subduction to collision and intracontinental extension (Rocchi et al., 2011).

7 Conclusions

Based on the detailed geological field investigation and geochemical and geochronological analyses on four types of magmatic rock (basalt, syenite, mafic veins, and granite veins) on Inexpressible Island, Northern Victoria Land, we conclude the following:

(1) Two stages of magmatic activity dominated by basalt and syenite formation are identified in the Terra Nova Complex, Northern Victoria Land.

(2) The middle to late Cambrian basalt and granitic veins developed in an early magmatic arc setting, with zircon ages of 504.7 ± 3.1 and 495.5 ± 4.9 Ma, respectively.

(3) The Early Ordovician syenite and monzodiorite veins were formed in a collisional environment of late-stage orogeny, with zircon ages of 485.8 ± 5.7 and 478 ± 4 Ma, respectively.

(4) Northern Victoria Land likely underwent a tectonic transition from subduction to collision and intracontinental extension over a ~20 Ma period during the late Cambrian and Early Ordovician.

Acknowledgments This work was supported by the National Science Foundation of China (Grant no. 41530209), the Central Public Interest Scientific Institution Basal Research Fund (Grant no. JYYWF201819), and the Chinese Polar Environment Comprehensive Investigation & Assessment Program (Grant no. CHINARE2016-02-05). The authors gratefully acknowledge the Chinese Arctic and Antarctic Administration, Polar Research Institute of China and the 30th, 31st, and 32nd Chinese National Antarctic Research Expeditions. We thank Huijun Han and Xiaoping Yan for providing the aerial image map, and Prof. Xiaochun Liu, Prof. Chengli Zhang and Dr. Jiawei Cui for help with data analysis and interpretation. We are also grateful to the anonymous reviewers for their constructive and detailed reviews and suggestions on the manuscript.

References

Belousova E, Griffin W, O'Reilly S, et al. 2002. Igneous zircon: trace element composition as an indicator of source rock type. Contrib Mineral Petr, 143(5): 602-622.

Black L P, Kamo S L, Williams I S, et al. 2003. The application of SHRIMP to Phanerozoic geochronology; a critical appraisal of four zircon standards. Chem Geol, 200(1-2): 171-188.

Black, L P, Sheraton J W. 1990. The influence of Precambrian Source Components on the U–Pb Zircon age of a Palaeozoic Granite from Northern Victoria Land, Antarctica. Precambrian Res, 46: 275-293.

Boger S D. 2011. Antarctica—Before and after Gondwana. Gondwana Res,

19(2): 335-371.

Boger S D, Miller J M. 2004. Terminal suturing of Gondwana and the onset of the Ross–Delamerian Orogeny: the cause and effect of an Early Cambrian reconfiguration of plate motions. Earth Planet Sc Lett, 219(1): 35-48.

Borg S G, Stump E, Holloway J R. 1986. Granitoids of Northern Victoria Land, Antarctica: A reconnaissance study of field relations, petrography, and geochemistry//Stump E. Geological investigations in Northern Victoria Land. Washington, D.C.: American Geophysical Union as part of the Antarctic Research Series, 46: 115-188.

Borsi L, Petrini R, Talarico F, et al. 1995. Geochemistry and Sr-Nd isotopes of amphibolite dykes of northern Victoria Land, Antarctica. Lithos, 35: 245-259.

Capponi G, Crispini L, Meccheri M. 1999. Structural history and tectonic evolution of the boundary between the Wilson and Bowers terranes, Lanterman Range, northern Victoria Land, Antarctica. Tectonophysics, 312(2-4): 249-266.

Chen T Y, Shen Y B, Zhao Y, et al. 2008. Geological development of Antarctica and evolution of Gondwanaland. Beijing: The Commercial Press, 372 (in Chinese with English abstract).

Di Vincenzo G, Horton F, Palmeri R. 2016. Protracted (~30 Ma) eclogite-facies metamorphism in northern Victoria Land (Antarctica): Implications for the geodynamics of the Ross/Delamerian Orogen. Gondwana Res, 40: 91-106.

Elliot D H, Fanning C M. 2008. Detrital zircons from upper Permian and lower Triassic Victoria Group sandstones, Shackleton Glacier region, Antarctica: Evidence for multiple sources along the Gondwana plate margin. Gondwana Res, 13(2): 259-274.

Estrada S, Andreas L, Eckelmann K, et al. 2016. Continuous Neoproterozoic to Ordovician sedimentation at the East Gondwana margin—Implications from detrital zircons of the Ross Orogen in northern Victoria Land, Antarctica. Gondwana Res, 37: 426-448.

Farabee M J, Taylor E L, Taylor T N. 1990. Correlation of Permian and Triassic palynomorph assemblages from the central Transantarctic Mountains, Anarctica. Rev Palaeobot Palyno, 65(1-4): 257-265.

Federico L, Crispini L, Capponi G. 2010. Fault–slip analysis and transpressional tectonics: A study of Paleozoic structures in northern Victoria Land, Antarctica. J Struct Geol, 32(5): 667-684.

Federico L, Crispini L, Capponi G, et al. 2009. The Cambrian Ross Orogeny in northern Victoria Land (Antarctica) and New Zealand: A synthesis. Gondwana Res, 15(2): 188-196.

Giacomini F, Tiepolo M, Dallai L, et al. 2007. On the onset and evolution of the Ross-orogeny magmatism in North Victoria Land—Antarctica. Chem Geol, 240(1-2): 103-128.

Godard G, Palmeri R. 2013. High-pressure metamorphism in Antarctica from the Proterozoic to the Cenozoic: A review and geodynamic implications. Gondwana Res, 23(3): 844-864.

Goodge J W, Fanning C M, Bennett V C. 2001. U–Pb evidence of ~1.7 Ga crustal tectonism during the Nimrod Orogeny in the Transantarctic Mountains, Antarctica: implications for Proterozoic plate reconstructions. Precambrian Res, 112(3-4): 261-288.

Hagen-Peter G, Cottle J M. 2016. Synchronous alkaline and subalkaline magmatism during the late Neoproterozoic–early Paleozoic Ross orogeny, Antarctica: Insights into magmatic sources and processes within a continental arc. Lithos, 262: 677-698.

Jones L M, Faure G. 1967. Age of the Vanda porphyry dikes in Wright Valley, southern Victoria Land, Antarctica. Earth Planet Sc Lett, 3: 321-324.

Li X H. 1997. Geochemistry of the Longsheng ophiolite from the southern margin of Yangtze Craton, SE China. Geochem J, 31(5): 323-337.

Li X H, Qi C S, Liu Y, et al. 2005. Petrogeniesis of the Neoproterozoic bimodal volcanic rocks along the western margin of the Yangtze Block: New constrains from Hf isotopes and Fe/Mn ratios. Chinese Sci Bull, 50(21): 2481-2486.

Liu D, Jian P, Zhang Q, et al. 2003. SHRIMP dating of adakites in the Tulingkai ophiolite, Inner Mongolia: evidence for the Early Paleozoic subduction. Acta Geol Sin, 77(3): 317-327.

Ludwig K R. 2009. SQUID 2: a user's manual. Berkeley Geochronology Center Special Publication, 5: 110.

Merdith A S, Williams S E, Müller R D, et al. 2017. Kinematic constraints on the Rodinia to Gondwana transition. Precambrian Res, 299: 132-150.

Middlemost E A K. 1994. Naming materials in the magma igneous rock system. Earth-Sci Rev, 37(3-4): 215-224.

Palmeri R, Sandroni S, Godard G, et al. 2012. Boninite-derived amphibolites from the Lanterman-Mariner suture (northern Victoria Land, Antarctica): New geochemical and petrological data. Lithos, 140: 200-223.

Paulsen T S, Encarnación J, Grunow A M, et al. 2007. New age constraints for a short pulse in Ross Orogen deformation triggered by East–West Gondwana suturing. Gondwana Res, 12(4): 417-427.

Paulsen T S, Encarnación J, Grunow A M, et al. 2013. Age and significance of 'outboard' high-grade metamorphics and intrusives of the Ross orogen, Antarctica. Gondwana Res, 24(1): 349-358.

Paulsen T S, Encarnación J, Grunow A M, et al. 2015. Detrital mineral ages from the Ross Supergroup, Antarctica: Implications for the Queen Maud terrane and outboard sediment provenance on the Gondwana margin. Gondwana Res, 27(1): 377-391.

Peccerillo R, Taylor S R. 1976. Geochemistry of eocene calc-alkaline volcanic rocks from the Kastamonu area, Northern Turkey. Contrib. Miner Petrol, 58:63-81.

Perugini D, Poli G, Rocchi S. 2005. Development of viscous fingering between mafic and felsic magmas: evidence from the Terra Nova Intrusive Complex (Antarctica). Miner Petrol, 83: 151-16.

Rocchi S, Bracciali L, Di Vincenzo G, et al. 2011. Arc accretion to the early Paleozoic Antarctic margin of Gondwana in Victoria Land. Gondwana Res, 19(3): 594-607.

Rocchi S, Di Vincenzo G, Dini A, et al. 2015. Time–space focused intrusion of genetically unrelated arc magmas in the early Paleozoic Ross–Delamerian Orogen (Morozumi Range, Antarctica). Lithos, 232: 84-99.

Rocchi S, Tonarini S, Armienti P, et al. 1998. Geochemical and isotopic structure of the early Palaeozoic active margin of Gondwana in northern Victoria Land, Antarctica. Tectonophysics, 284(3-4): 261-281.

Sheraton J W, Babcock R S, Black L P, et al. 1987. Petrogenesis of granitic rocks of the Daniels Range, northern Victoria Land, Antarctica. Precambrian Res, 37: 267-286.

Song B, Zhang Y, Wan Y, et al. 2002. Mount making and procedure of the SHRIMP dating. Geol Rev, 48(Suppl.): 26-30 (in Chinese with English abstract).

Stump E, Fitzgerald P G. 1992. Episodic uplift of the Transantarctic Mountains. Geology, 20: 161-164.

Talarico F, Castelli D. 1995. Relict granulites in the Ross orogen of northern Victoria Land (Antarctica), I. Field occurrence, petrography and metamorphic evolution. Precambrian Res, 75(3): 141-156.

Talarico F, Borsi L, Lombardo B. 1995. Relict granulites in the Ross Orogen of northern Victoria Land (Antarctica), II. Geochemistry and palaeo-tectonic implications. Precambrian Res, 75(3): 157-174.

Vetter U, Tessensohn F. 1987. S- and I-type granitoids of North Victoria Land, and their inferred geotectonic setting. Geol Rundsch, 76: 233-243.

Vincenzo G D, Rocchi S. 1999. Origin and interaction of mafic and felsic magmas in an evolving late orogenic setting: the Early Paleozoic Terra Nova Intrusive Complex, Antarctica. Contrib Mineral Petrol, 137: 15-35.

Wang W, Hu J M, Chen H, et al. 2014. LA-ICP-MS zircon U-Pb ages and geological constraint of intrusive rocks from the Inexpressible Island, Northern Victoria Land, Antarctica. Geol Bull China, 33(12): 2023-2031 (in Chinese with English abstract).

Weaver S D, Bradshaw J D, Laird M G. 1984. Geochemistry of Cambrian volcanics of the Bowers Supergroup and implications for the Early Palaeozoic tectonic evolution of northern Victoria Land, Antarctica. Earth Planet Sc Lett, 68: 128-140.

Yang J, Wang J R, Zhang Q, et al. 2016. Global IAB data excavation: The performance in basalt discrimination diagrams and preliminary interpretation. Geol Bull China, 35(12): 1937-1949 (in Chinese with English abstract).